

Deep Learning Models for Flood Predictions in South Florida

Jimeng Shi^{1†}, Zeda Yin^{2†}, Rukmangadh Sai Myana¹, Khandker Ishtiaq³, Anupama John³,
Jayantha Obeysekera³, Arturo S. Leon^{2‡}, Giri Narasimhan^{1‡}

¹Knight Foundation School of Computing and Information Sciences, Florida International University

²Department of Civil and Environmental Engineering, Florida International University

³Sea Level Solutions Center, and Department of Earth and Environment, Florida International University

{jshi008, zyin005, rmyan001, arleon, kishtiaq, anujohn, jobeysek, giri}@fiu.edu

[†]Equal Contributions, [‡]Corresponding Author

Abstract

Simulating and predicting water levels in river systems is essential for flood warnings, hydraulic operations, and flood mitigations. In the engineering field, tools such as HEC-RAS, MIKE, and SWMM are used to build detailed physics-based hydrological and hydraulic computational models to simulate the entire watershed, and thereby predicting the water stage at any point in the system. However, these physics-based models are computationally intensive, especially for large watersheds and for longer simulations. To overcome this problem, we train several deep learning (DL) models for use as surrogate models to rapidly predict water stage. The downstream stage of the Miami River in South Florida is chosen as a case study for this paper. The dataset is from January 1, 2010, to December 31, 2020, downloaded from the DBHYDRO database of the South Florida Water Management District (SFWMD). Extensive experiments show that the performance of the DL models is comparable to that of the physics-based models, even during extreme precipitation conditions (i.e., tropical storms). Furthermore, we study the decline in prediction accuracy of the DL models with increase in prediction lengths. In order to predict the water stage in the future, our DL models use measured variables of the river system from the recent past as well as covariates that can be reliably predicted in the near future. In summary, the deep learning models achieve comparable or better error rates with at least 1000x speedup in comparison to the physics-based models.

Keywords: Deep learning; Physics-based model; Water level/stage prediction; Future covariates.

1. Introduction

Floods are one of the most common natural phenomena caused by increased flow rate and water stage in a river resulting in temporarily submerging any low-lying areas along its banks (Parhi, 2018). Increasing extreme rainfall due to climate change along with the increasing trends in urban development will likely increase the frequency and volume of floods (NASA, 2017; Mynett & Vojinovic, 2009). Floods result in commercial losses and dangers to human life (Grothmann & Reusswig, 2006; Hirabayashi & Kanae, 2009; Alexander et al., 2019) and could contribute to environmental and public health risks (Okaka & Odhiambo, 2018; Rivett et al., 2022). Thus, knowing the time and location of floods ahead of time is critical for hydraulic structure operators to make informed decisions for flood mitigation in a timely manner (Kusler,

2004; Leon et al, 2020) and for citizens and local governments to be better prepared for eventualities. Detailed and accurate numerical models are currently available to simulate river floods, including Hydrologic Engineering Center's River Analysis System (HEC-RAS) (Hydrologic Engineering Center, 2016), MIKE (The Academy by DHI, 2023) and SWMM (Huber 1985). However, there are applications (e.g., finding the optimal flow release at the control gates to minimize flooding) where thousands of simulations of these physics-based models are required to find the optimal flow release on the control gate to mitigate the flow (Leon et al., 2020; Leon et al., 2021). Using conventional physics-based models for real-time optimal flood control is therefore infeasible. There is a critical need for a surrogate model that can rapidly and accurately predict the water levels at specific locations along the river as a function of time.

Multiple related studies have been conducted on the prediction of hydrological and hydraulic relations and parameters by using classic machine learning models (Sadler et al., 2018; Sajedi-Hosseini et al., 2018; Gorgoglione et al., 2021; Abdalla et al., 2021; Adnan et al., 2021). Various application-level case studies adapted machine learning models, including support vector machines (Kisi et al., 2019), logistic regression (Zhao et al., 2019), and random forest (Kim et al., 2020), to predict the hydrological and hydraulic relationships in the past years. These studies showed that machine learning (ML) models have the capability to predict hydrological and hydraulic relationships with reasonable accuracy. With the era of big data that started in recent years, deep learning (DL) models have been used in many different research fields and have achieved impressive performance. The accuracy of flood inundation prediction was improved by artificial neural networks (Tamiru & Dinka, 2021), even though they built a hybrid model combining DL models and HEC-RAS. Amasyali & El-Gohary, 2017 applied a traditional ML model (support vector machines), a DL model (artificial neural networks), and other statistical regression algorithms to predict building energy consumption. Notably, some deep learning models involving time series forecasting were employed in many fields as well. Air quality, electric consumption and water levels in future period were predicted using several DL models, including recurrent neural networks, long short-term memory, gated recurrent units and their variants (Shi et al., 2022; Shi et al., 2023). Kiprijanovska et al, 2020, predicted day-ahead household electrical energy consumption using residual neural network. Yamak et al., 2019, worked on the predictions of Bitcoin's price as a function of time and compared the performance of ARIMA, long short-term memory and gated recurrent units accordingly. Rainfall-runoff (Adnan et al., 2021) and overflow in combined sewer systems (Yin et al., 2022) were predicted using long short-term memory. Although the above DL models have been applied to problems from diverse domains, these methods failed to incorporate (reliably predictable) future covariates into their models.

The objective of this paper is to develop DL models to simulate and predict water stage at several locations in the watershed. We show that when the future covariates are incorporated into our DL models, they perform well even during extreme conditions (i.e., tropical storm events). Besides, a DL model combining recurrent neural networks (RNN) and convolutional neural networks (CNN) was also developed, which outperforms all other DL models in our paper. Compared to physics-based models, the surrogate DL models presented in this paper can predict water stages rapidly and with reasonable accuracy. This is likely to greatly impact applications such as optimal flood control. We also discuss the impact of prediction length while using DL models and analyze which DL models perform better with different prediction lengths. Lastly, DL models can output responses that are as accurate and consistent as HEC-RAS, even when boundary conditions are changed.

2. Methodology and Modeling

In this section, we present the methodology used in this paper, describing the data acquisition, data processing, the HEC-RAS models, and the DL models.

2.1 Study area and Dataset

2.1.1 Study area

The Miami River is one of the largest rivers in South Florida emptying into the Biscayne Bay. A large metropolis with a sizable population and many commercial enterprises are located along the river. South Florida is also vulnerable to hurricane events with extremely heavy precipitation (Azzi et al., 2020). Given its vulnerability to flooding and the need to protect the security and economy of the region it impacts, the Miami River provides an excellent data set for a case study in this paper. The schematic of the research area is shown in Figure 1, and the red box shows the boundary of this study domain. The study area consists of 5.6 miles of the last part of the Miami River, its two tributaries: C4 (upper) and C6 (lower), and three water stations, S25A, S25B, and S26 located 1.13 miles, 0.94, and 5.61 miles upstream away from mainstream junctions of C6 and C4, respectively, and three hydraulic structures (including spillway gates, culverts, and pumps) used to manage the flows. The water stages and flow rates of the Miami River are greatly influenced by tides and the various hydraulic structures along its course. The mouth of the river is located on the Biscayne Bay, which explains why the downstream water stage is strongly influenced by the tides in Biscayne Bay. The hydraulic structures avoid seawater flowing back from the Biscayne Bay and therefore have a significant impact on the state of the river system.

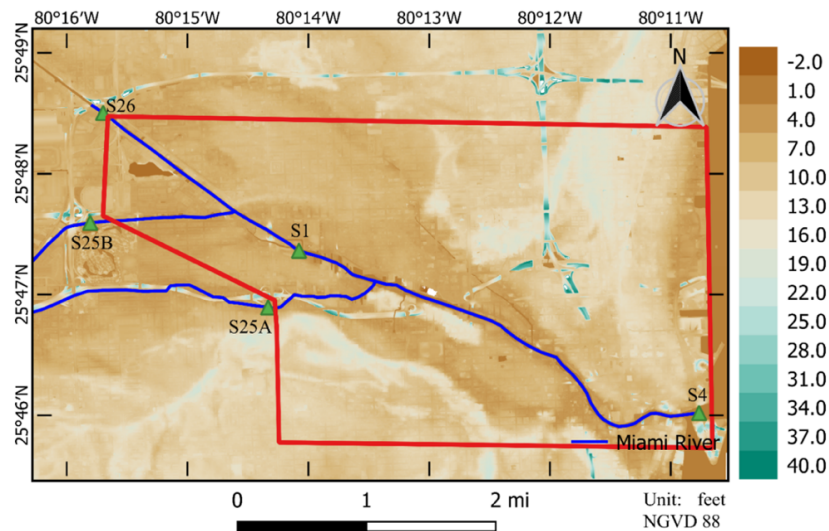


Figure 1. Map of the study area in Miami, FL, showing the shape of the downstream of Miami river, hydrological stations, and the region of study marked in red. The legend represents the elevation of the Datum NAVD 88.

2.1.2 Data acquisition and description

The river data used in this paper was collected hourly over a period of 11 years (Jan 1, 2010 to Dec 31, 2020) at five water stations (S1, S4, S25A, S25B, and S26 shown in Figure 1) and retrieved from DBHYDRO, the South Florida Water Management District's (SFWMD) database. The rainfall data is pixel-based (gridded) radar precipitation data retrieved from the Next Generation Weather Radar (NEXRAD) system data archived by SFWMD. The precipitation data was collected every hour and converted from the raw dataset using forward interpolation method. The water stage and precipitation features used by both HEC-RAS and DL models are described in Table 1. The water stage at S1 and tail water stage at S25A, S25B, S26 were identified as target variables to predict. Other features were additional covariates that can influence the prediction of the target variables for the future. In particular, gate openings or pump flows at

upstream locations (S25A, S25B, S26) and water stage at downstream (S4) are set as “boundary conditions” in the HEC-RAS model. Water station S26 is a water station with a gated spillway and a set of pumps. Station S25B has two spillway gates that work independently and a set of pumps. The gate and pump flow measurements are the total flow through the gate and pump, respectively. Station S25A has a culvert structure (with a control gate), which is recorded. Stations S1 and S4 are water stations that are used to record and monitor the water stage.

Table 1. Description of data feature and usage

Description	Abbreviation	Unit	Target variables
S26 gate flow	Flow_S26	cubic feet / second	
S26 pump flow	Pump_S26	cubic feet / second	
S26 tailwater stage	TWS_S26	cubic feet / second	target
S25A gate flow	Flow_S25A	cubic feet / second	
S25A tailwater stage	TWS_25A	feet	target
S25B total gate flow	Flow_S25B	cubic feet / second	
S25B pump flow	Pump_S25B	cubic feet / second	
S25B tailwater stage	TWS_S25B	feet	target
S1 water stage	WS_S1	feet	target
S4 water stage (tide info)	WS_S4	feet	
Mean gridded precipitation intensity	Grid_Rainfall	inches / hour	

2.1.3 Data pre-processing for Deep Learning Models

Unlike for the HEC-RAS model, data for the DL models need to be pre-processed beforehand. The data were normalized to avoid gradient values from exploding or vanishing (i.e., becoming infinity or zero). Min-Max normalization technique was used as shown in Eq. (1):

$$x' = \frac{x - x_{min}}{x_{max} - x_{min}} \quad (1)$$

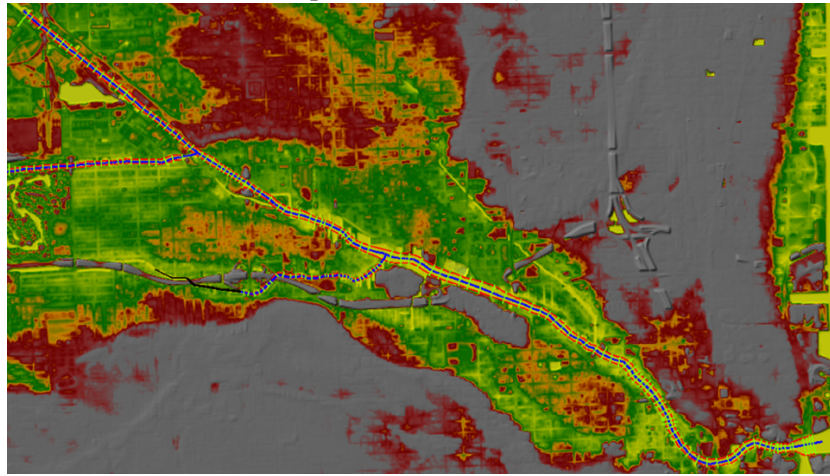
where the minimum value was set to 0, the maximum to 1, and all other values were linearly scaled as shown in (1). The dataset was divided into 80% training (Jan 1, 2010 to Aug 7, 2018) and 20% test set (Aug 8, 2018 to Dec 31, 2020).

2.2 HEC-RAS Model

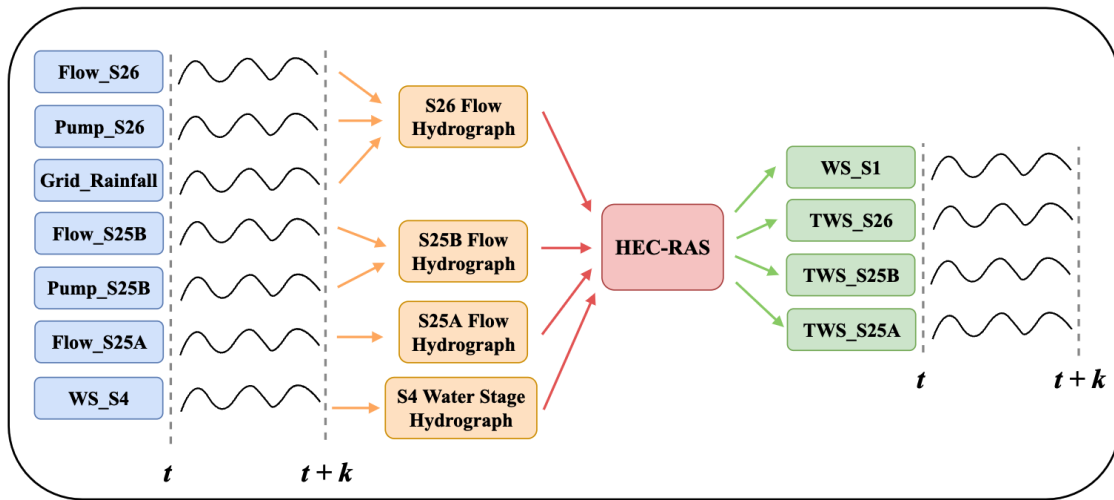
The detailed physics-based model was simulated by the most used tool: HEC-RAS, which can be used by either solving 1D unsteady diffusion wave equations or by solving full shallow water equations. According to the HEC-RAS manual, a full momentum-based equation set must be included to simulate tidally influenced conditions. Thus, full shallow water equations were employed to solve the flow domain in this work. The geographic digital elevation model (DEM) used in HEC-RAS model is shown in Figure 2a along

with a schematic of the treatment of the variables to create boundary conditions in HEC-RAS, as shown in Figure 2b. The bathymetry data was retrieved from Statewide Model Management System (SMMS) and used to modify the DEM model. In this work, a 1D-2D coupled computational domain was used to calculate the overland flow more accurately during the heavy rainfall event. The mesh size for the 2D area was set to 40X40 feet². Four boundary conditions were required to run the HEC-RAS model: three upstream conditions (at S26, S25A, and S25B) and one downstream condition (at S4). All three upstream conditions were set as flow hydrographs. As shown in Figure 2b, the upstream flow hydrograph was set to the gate flow value, with an added pump flow value, if there was a pump station. In HEC-RAS, the unweighted average of the gridded precipitation data was converted based on hydrological calculations and was added to the boundary conditions at station S26.

Since the HEC-RAS model is a conventional numerical solver for shallow water equations, the input data (boundary conditions) of HEC-RAS had the same period ($t + 1$ to $t + k$) as the output data, and there was no lag time data needed in the model. A 2-year long simulation (from Jan 1, 2019, 00:00 to Dec 31, 2020, 23:00) was completed using HEC-RAS and was used to compare with prediction results of DL models. The computation time step size was set at 1 minute to keep the computation stable, and the output interval was set the same as for the DL computations (i.e., 1h)



(a)



(b)

Figure 2. (a) Raster map of the study area; (b) Schematic of the variables and the hydrographs that were used as boundary conditions of the HEC-RAS model.

2.3 Deep Learning Models

Four single DL models were used in this paper, including Recurrent Neural Networks (RNN), Long Short-Term Memory networks (LSTM), Multilayer Perceptron (MLP) and Convolutional Neural Networks (CNN). A DL model combining RNN and CNN in series was also developed to capture temporal and spatial information. The overall framework for the DL models is shown in Figure 3. The significant difference between the models is that predicting water stage with DL models depends on the past information (e.g., looking back w timesteps of all the variables), future predictable information (e.g., k timesteps of rainfall data in the future), and human-controlled information (e.g., flow rate scheduled through gate or pump for the k timesteps), while HEC-RAS only requires the last two. In other words, HEC-RAS only needs the boundary conditions for the prediction period, while DL models were designed to use both the information from the desired period as well as the data from the recent past.

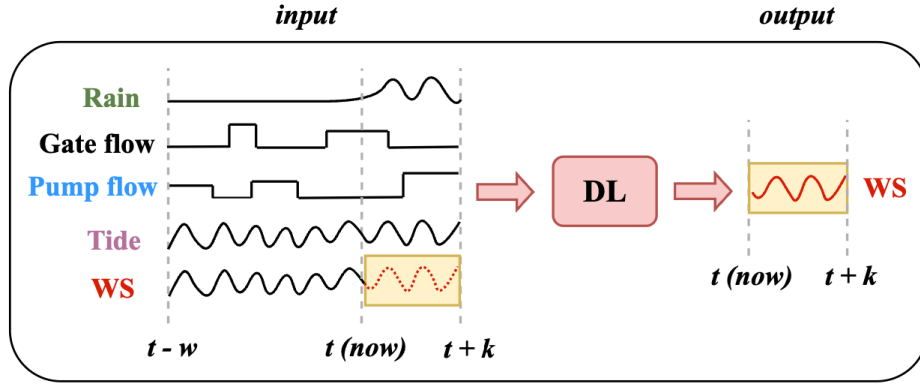


Figure 3. Overall framework of the DL models. Vertical dashed lines indicate time points of interest.

Input data is shown as a set of time series to the left of the schematic, while the output to predict is shown as a yellow shaded box.

As shown in Figure 3, we assume that the current time is represented by time t , and w and k are the lengths of the history considered and the length of the forecast horizon, respectively. WS is a vector representing the (combined) water stage time series for S1, S25A tailwater, S25B tailwater, and S26 tailwater. Gate flow refers to the amount of water flowing through the gate and Pump flow represents the amount of pumped water, both representing a time series. Tide is the water stage at S4, i.e., the sea level information. For each location, we seek to predict the water stage from time $t + 1$ to $t + k$. Therefore, all covariates (rain, tide, gate flow, pump flow) from $t + 1$ to $t + k$ were considered using predicted or scheduled information. Rain and tide forecasts are available from the weather forecasting agency and oceanographic agency, while gate flow and pump flow are assumed to have been provided by the water management agency. DL models are also provided with historical data (rain, gate flow, pump flow, tide water stage) from time $t - w$ to t , with the assumption that recent past information informs us of the “state of the system”. Mathematically, the DL model is described as follows:

$$WS_{[t+1,t+k]}^i = f(WS_{[t-w,t]}, Tide_{[t-w,t+k]}, Rain_{[t-w,t+k]}, GF_{[t-w,t+k]}, PF_{[t-w,t+k]}), \quad (2)$$

where $WS_{[t+1,t+k]}^i$ is water stage at the i^{th} station from time $t + 1$ to $t + k$, $i \in \{S1, S25A, S25B, S26\}$; $WS_{[t-w,t]}$ is a vector representing water stages for all four locations from time $t - w$ to t ; $Tide_{[t-w,t+k]}$ is water stage at S4 from time $t - w$ to $t + k$; $Rain_{[t-w,t+k]}$ is the mean gridded rainfall for the study domain from time $t - w$ to $t + k$; $GF_{[t-w,t+k]}$, $PF_{[t-w,t+k]}$ represent water flowing through gate and pump respectively for all four stations from time $t - w$ to $t + k$.

2.3.1 Multilayer Perceptron (MLP)

MLP is a modification of the simple perceptron and is a part of the family of the fully connected feedforward neural networks. MLP is well suited to extract global non-linear relationships between features (Del Campo et al., 2021) since it has multiple hidden layers used for non-linear computation, and these layers are fully connected. MLP consists of at least three layers: one input layer, one or multiple hidden layers, and one output layer. The input layer is used to load input features to be processed. Hidden layers and the output layer are used for intermediate non-linear computations (so-called “black box”) and the prediction output, respectively. Each node of hidden layers includes a summation and activation computation. Mathematically, it is described as follows:

$$\begin{aligned}
 \mathbf{h}_1 &= \sigma(W_1 \cdot \mathbf{x} + \mathbf{b}_1); \\
 \mathbf{h}_2 &= \sigma(W_2 \cdot \mathbf{h}_1 + \mathbf{b}_2); \\
 &\dots \dots \\
 \mathbf{h}_l &= \sigma(W_l \cdot \mathbf{h}_{l-1} + \mathbf{b}_l); \\
 \mathbf{y} &= \sigma(W_{l+1} \cdot \mathbf{h}_l + \mathbf{b}_{l+1}),
 \end{aligned} \tag{3}$$

where x is a flattened vector as input and w is the length of time from which past information is used. The input layer is the 0^{th} layer, hidden layers h_1, h_2, \dots, h_l are the next l layers, and output layer is the $(l + 1)^{th}$ layer, $W_j \in \mathbb{R}^{n(j) \times n(j-1)}$ is the parameter matrix from the $(j - 1)^{th}$ hidden layer to j^{th} hidden layer, $n(j)$ is the number of neurons of j^{th} layer; $b_j \in \mathbb{R}^{n(j)}$ is the bias vector of j^{th} layer.

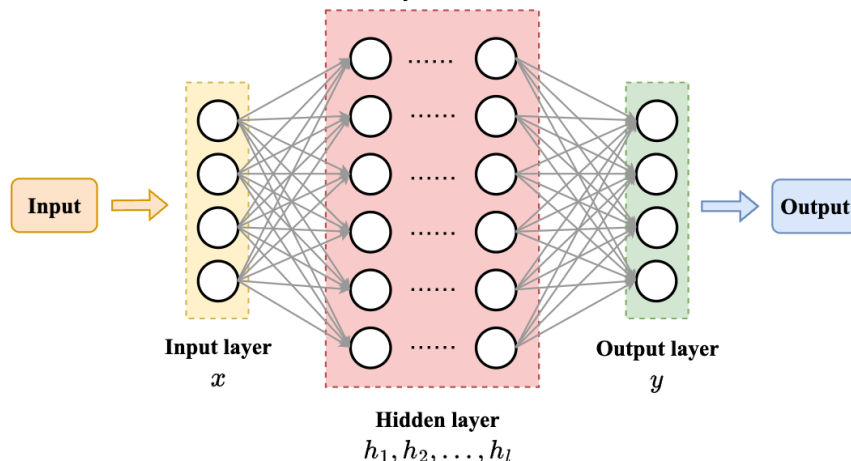


Figure 4. Architecture of Multilayer Perceptron

2.3.2 Recurrent Neural Networks (RNNs)

RNN is one of the classic DL models, which is well suited for the sequential data (e.g., water level changing over time). It can learn temporal dependencies between input features from the recent past and the target variables in the future by recurrently training and updating the transitions of an internal (hidden) state from the last timestep to the current timestep. In our case, we incorporate related future variables as well.

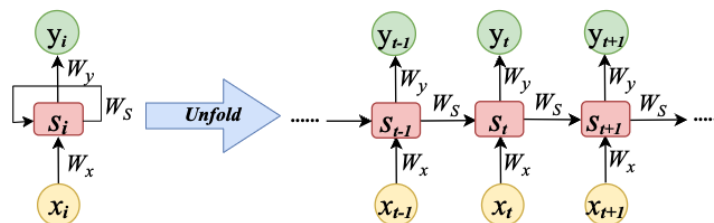


Figure 5. Architecture of RNNs

Figure 5 shows that RNNs can memorize what has already been processed before time t and save the information in the hidden state S_{t-1} . RNNs combine current information, x_t , in state S_t , to generate output y_t . The comparison with the ground truth of y_t allows RNNs to learn from previous iterations. The training process is determined by 3 parameter matrices W_x , W_s , W_y , and two bias vectors b_s , b_y . The simplified description of RNNs is that they propagate forward, predict output, and compute prediction errors. To minimize the errors, RNNs backpropagate the computed errors to update the gradients at each timestep and update weights for the next iteration. The computational process of each hidden state (unit or cell) is described in Figure 6. Mathematically, it is given as follows:

$$\begin{aligned} S_t &= \tanh(W_{xs} \cdot (x_t \oplus S_{t-1}) + b_s) \text{ and} \\ y_t &= \sigma(W_y \cdot S_t + b_y), \end{aligned} \quad (4)$$

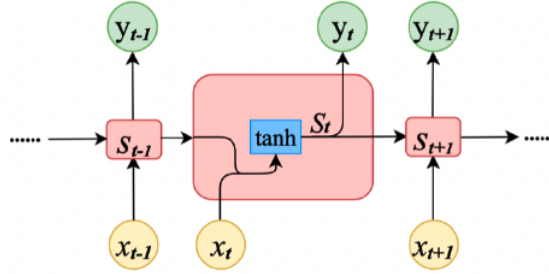


Figure 6. Architecture of RNNs

where $x_t \in \mathbb{R}^m$ is the input vector of m input features at time t ; $W_{xs} \in \mathbb{R}^{n \times (m+n)}$ and $W_y \in \mathbb{R}^{n \times n}$ are parameter matrices; n is the number of neurons in the RNN layer; $b_s \in \mathbb{R}^n$ and $b_y \in \mathbb{R}^n$ are bias vectors for the internal state and output, respectively; σ is the sigmoid activation function; S_t is the internal (hidden) state; and $x_t \oplus S_{t-1}$ is the concatenation of vectors, x_t and S_{t-1} .

2.3.3 Long Short-term Memory (LSTM)

Due to recurrently repeated multiplication of the parameter matrices, RNNs are prone to vanishing gradients, causing them to run out of memory. To mitigate this problem, LSTM networks were proposed as a variant of RNNs. As shown in Figure 7, at time t , an LSTM includes a cell state, C_t , which runs straight along the entire chain with only some linear interactions. LSTMs also have hidden states, S_t , representing the information from the past timesteps and the information that is filtered/updated with the new input x_t by the following gate operations. LSTM can learn slightly longer time dependencies by incorporating forget gates, f_t , input gates, i_t , additional gates, c_t , and output gates, o_t , to control the inflow, filtering, and outflow of past and current information. The above gates can help the models to alleviate the vanishing gradient problem to some extent. The mathematical formulation is as follows:

$$\begin{aligned} f_t &= \sigma(W_f \cdot (x_t \oplus S_{t-1}) + b_f); \\ i_t &= \sigma(W_i \cdot (x_t \oplus S_{t-1}) + b_i); \\ \tilde{C}_t &= \tanh(W_c \cdot (x_t \oplus S_{t-1}) + b_c); \\ C_t &= f_t \cdot C_{t-1} + i_t \cdot \tilde{C}_t; \\ O_t &= \sigma(W_o \cdot (x_t \oplus S_{t-1}) + b_o); \\ S_t &= \tanh(C_t) \cdot O_t; \text{ and} \\ y_t &= \sigma(W_y \cdot S_t + b_y), \end{aligned} \quad (5)$$

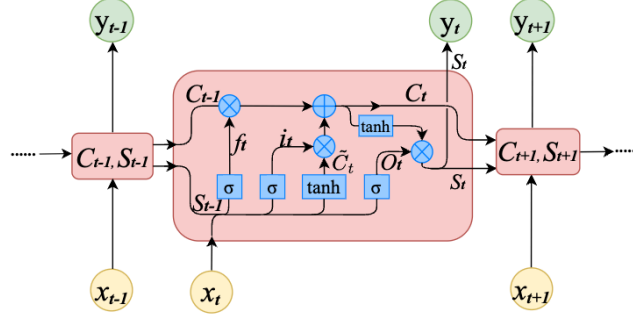


Figure 7. Architecture of LSTMs

where $\mathbf{x}_t \in \mathbb{R}^m$ is the vector of m input features at time t ; $W_f, W_i, W_C, W_O \in \mathbb{R}^{n \times (m+n)}$ and $W_y \in \mathbb{R}^{n \times n}$ are parameter matrices; n is the number of neurons in the LSTMs layer; $b_f, b_i, b_C, b_O, b_y \in \mathbb{R}^n$ are bias vectors; σ is the sigmoid activation function; and S_t is the internal (hidden) state. The functions f_t, i_t, \tilde{C}_t , and O_t are implemented by a forget gate, input gate, addition gate, and output gate, respectively.

2.3.4 Convolutional Neural Networks (CNNs)

CNNs are classical neural networks designed with convolution kernels, which are used to extract local spatial features and create informative representations of time series. CNNs extract high-level features by sliding a filter convolution kernel (weight matrix) over the input time series and at each point doing convolutional computation (i.e., dot product between the convolution kernel and the input time series) (Borovykh et al., 2018). Each convolutional layer is followed by a maximum pooling layer, which is used to extract the most meaningful values of each convolutional computation. Due to the pooling layer, CNNs might work well on some time series even with noise. Such structures allow the model to learn these kernels that can represent certain specific patterns of the input series data and infer the future values with these patterns. Besides, the local perceptron and weight sharing of CNNs can greatly reduce the number of parameters such that the learning process is accelerated. The detailed convolutional computation can be found in (Keren & Schuller, 2016, Borovykh et al., 2017).

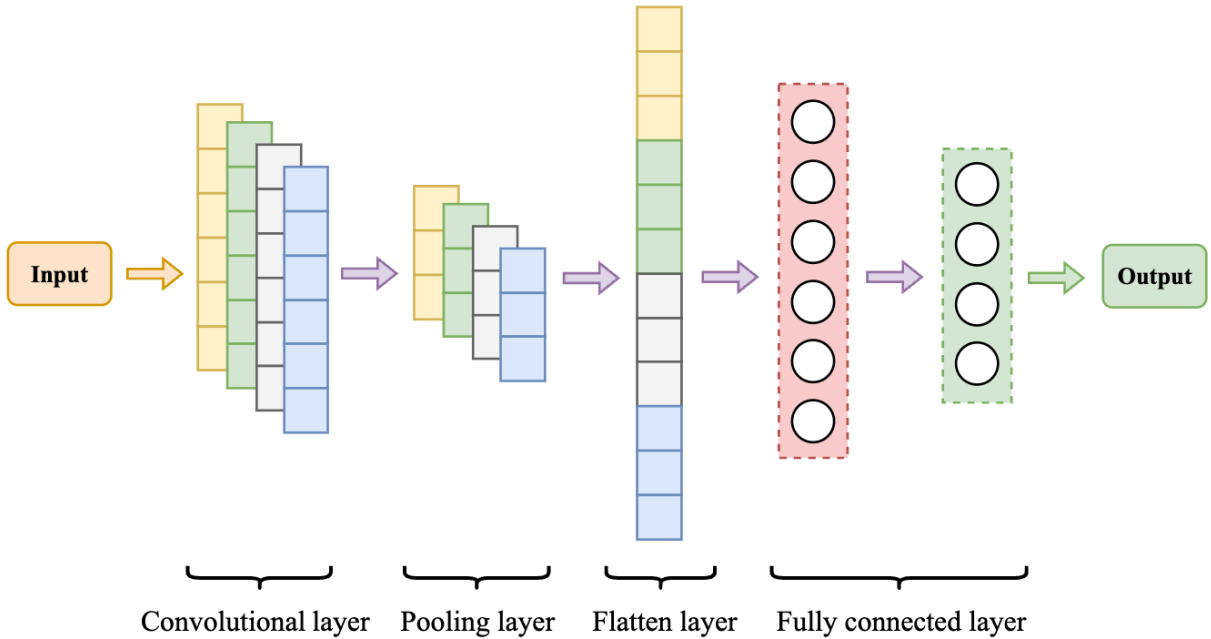


Figure 8. Architecture of Convolutional Neural Networks

As shown in [Figure 8](#) above, there are several feature vectors in convolutional layers since these layers operate convolutional computations using multiple kernels. Each convolutional computation with one kernel corresponds to one feature vector. A pooling layer is used to distill the output of the convolutional layer to the most salient elements by obtaining the maximum value in each pooling window. There is also an average pooling layer, which compute average value of each pooling window. Max pooling is used in our paper. The convolutional and pooling layers are followed by a flattened layer which maps the convolutional features to a single one-dimensional vector. Flatten layer is used merely to transform the data shape to satisfy the input requirement for the later layers. The fully connected layers interpret those features extracted by the convolutional layers and output the predictions.

2.3.5 Combination of RNN & CNN: RCNN

As we mentioned in Section 2.3.3, RNNs are best suited for sequential DL to learn a short-term temporal dependency, but they fail to learn the functional relationships across long time intervals. In Section 2.3.4, we presented CNNs that have the powerful ability to learn local spatial relationships ([Keren & Schuller, 2016](#)) among variables, thus reducing the length of the time series and mitigating the memory issue of RNNs. Considering the characteristics of the above two models, we will present a conjoint deep learning model by combining Convolutional Neural Networks (CNNs) and Recurrent Neural Networks (RNNs) in series. With the help of CNNs, the temporal features extracted by RNNs continue to be learned by CNNs. Hence, spatial relationship between variables is learned as well. At the same time, a pooling layer can extract most salient features with temporal and spatial characteristics. Based on an enhanced feature extraction, RCNN models can generate more accurate predictions for a longer period. The architecture of RCNN model has been shown in [Figure 9](#). Explanations for convolutional and pooling layers are the same as that in [Figure 8](#).

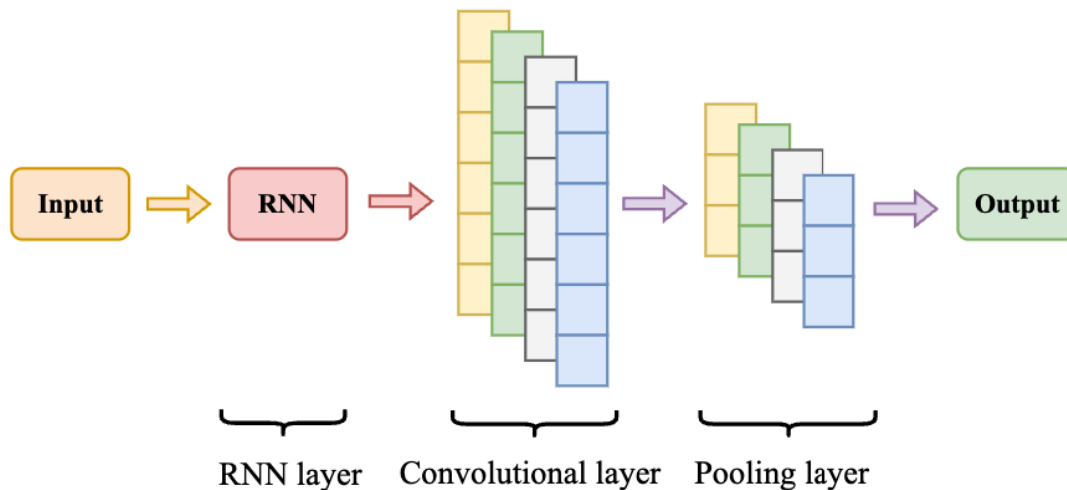


Figure 9. Architecture of Convolutional-RNNs

3. Results

For DL models, we used all the measured variables from the past 168 timesteps (7 days) and all the predictable and determinate covariates (precipitation and gate releases) from the future 24 timesteps (1 day) as input data, with the intent to predict target variables (water stage at S1, S25A, S25B, S26) for the future 24 timesteps (1 day). After training DL models with the training set, we applied these models to the test set (2019-2020) and compared the predicted water stages with the simulated water stages of HEC-RAS and

the observed water stages from the measuring stations. In the following discussion, we represent the k^{th} predicted timestep in the future with $t + k$ hour prediction. For example, $t + 24$ hour prediction refers to the predicted timestep 24 hours in the future.

3.1 Output performance analysis

3.1.1 Performance analysis on prediction timesteps

As mentioned above, DL models in this paper were set to predict the target variables from $t + 1$ hour to $t + 24$ hours. In this subsection, we show the prediction results for $t + 1$, $t + 12$, $t + 18$, $t + 24$ hours. The HEC-RAS model is not comparable since it does not make future predictions, but computes one timestep of output when the appropriate input is fed. Therefore, the HEC-RAS model will not be compared here. To measure the performance of the DL models, mean absolute errors (MAE) and root mean square error (RMSE) were used. The corresponding equations are expressed as Eq. (6) and Eq. (7).

$MAE = \frac{\sum_{i=1}^n Y_{prediction} - Y_{true} }{n},$	(6)
$RMSE = \sqrt{\frac{\sum_{i=1}^n (Y_{prediction} - Y_{true})^2}{n}},$	(7)

where $Y_{prediction}$, Y_{true} represent the model outputs and ground truth data, respectively, and n stands for the number of samples.

Table 2. Mean Absolute Error (MAE) of the DL models of all locations (S1, 25A, S25B, S26) at different prediction timesteps (hours)

	1-hr ahead	8-hr ahead	16-hr ahead	24-hr ahead	Entire time interval
MLP	0.161	0.167	0.148	0.157	0.151
RNN	<i>0.075</i>	<i>0.093</i>	0.145	0.148	0.120
LSTM	0.098	0.147	0.165	0.152	0.148
CNN	0.102	0.120	<i>0.118</i>	<i>0.124</i>	<i>0.118</i>
RCNN	<i>0.097</i>	<i>0.094</i>	<i>0.099</i>	<i>0.106</i>	<i>0.098</i>

Table 3. Root Mean Square Error (RMSE) of the DL models of all locations (S1, 25A, S25B, S26) at different prediction timesteps (hours)

	1-hr ahead	8-hr ahead	16-hr ahead	24-hr ahead	Entire time interval
MLP	0.206	0.205	0.183	0.197	0.191
RNN	<i>0.098</i>	<i>0.126</i>	0.185	0.192	0.158
LSTM	<i>0.124</i>	0.198	0.218	0.202	0.200
CNN	0.130	0.153	<i>0.151</i>	<i>0.157</i>	<i>0.150</i>
RCNN	0.128	<i>0.122</i>	<i>0.130</i>	<i>0.140</i>	<i>0.129</i>

Note: Numbers in Bold and Italic fonts represent the lowest error in column; Bold fonts refer to the second lowest error.

The MAE and RMSE values in Table 2 and Table 3 show the prediction errors of DL models as a function of prediction length. All DL models had an acceptable error range in terms of both MAE and RMSE. The combined model (RCNN) produced the last MAE and in four out of five cases for the RMSE

measure. The classical models (RNN, LSTM) were more sensitive to the prediction length, performing well for short-term predictions (1-hr and 8-hr), but suffered larger errors for longer time predictions. In contrast, MLP and CNN were relatively insensitive to prediction length, displaying stable MAE with low variance even for longer predictions. Thus, simpler DL models are adequate for short prediction lengths, but MLP and CNN work better for longer prediction lengths. The combined model, RCNN, displays lower errors for both the short-term as well as the longer-term predictions. Lastly, it was surprising to note that LSTMs did not outperform RNNs, even though they are considered as an improved version of RNNs.

To evaluate the performance of these DL models, we also analyzed the actual prediction errors with 24 hours ahead. They are computed as $Y_{prediction} - Y_{true}$ for the test set. Violin plots were used to visualize the distribution of prediction errors (see Figure 10). Violin plots display the density distribution along with the median value, the peak value, the 25th percentile and the 75th percentile (see top and bottom of the small black box inside). The bigger the belly of the violin plot, the more errors are distributed in that corresponding area.

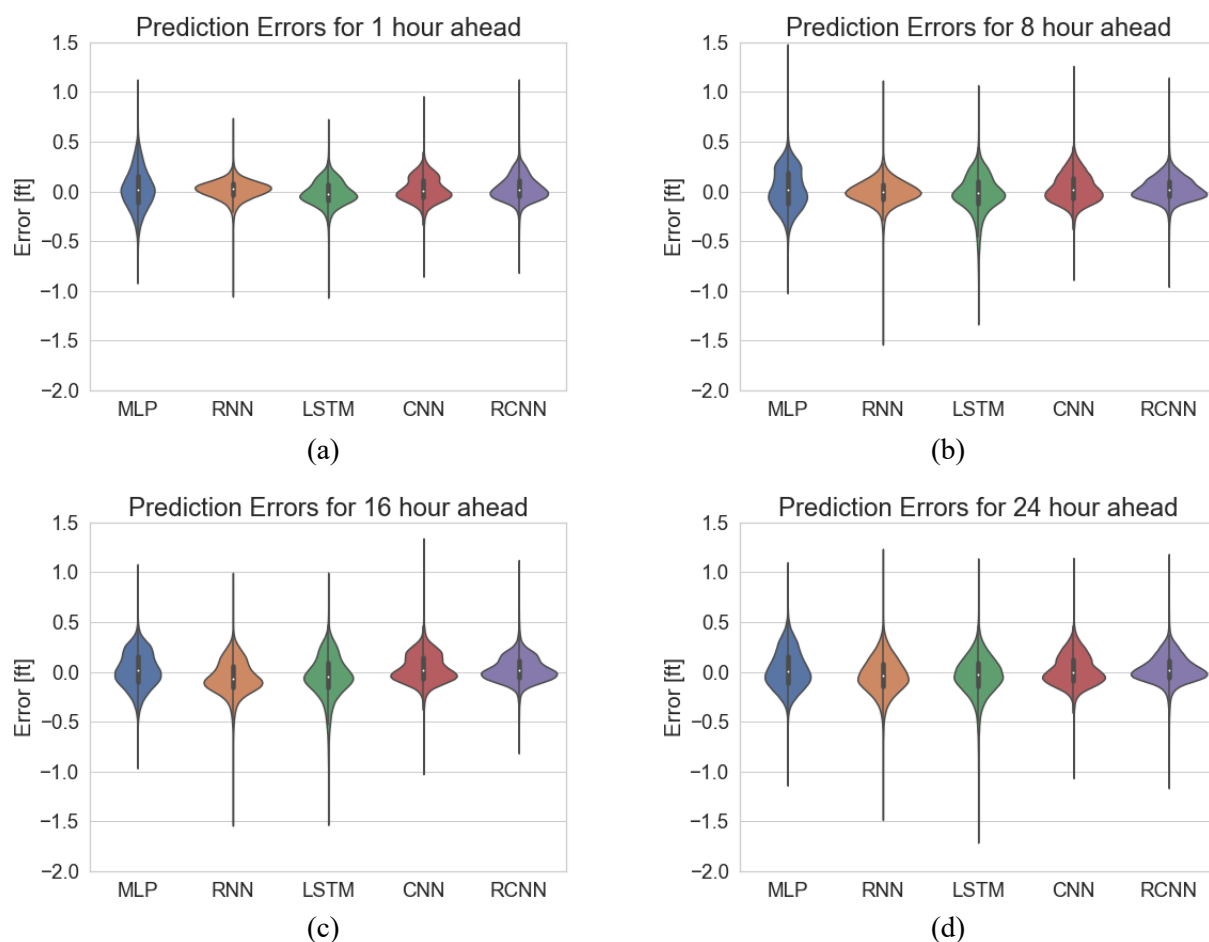


Figure 10. Violin plots showing density distributions of actual errors for the five DL methods at all locations with prediction length: (a) 1 hour; (b) 12 hours; (c) 18 hours; and (d) 24 hours.

From Figure 10, we conclude that most errors are distributed close to the 0 value, which means DL models produce mildly biased prediction results. If the acceptable error range is $(-0.5, 0.5)$ feet, only a small percentage of errors are outside this range. Such “*Spike errors*” occur when heavy precipitation happens

within a short period of time. Table 4 shows that the RCNN model has the lowest percentage (0.803%) of prediction errors outside (-0.5, 0.5) feet at all stations of interest (S1, S25A, S25B, S26).

Table 4. Percentage of actual prediction errors beyond acceptable range (-0.5, 0.5) feet

	1-hr ahead	8-hr ahead	16-hr ahead	24-hr ahead	Entire time interval
MLP	1.533 %	0.801 %	0.326 %	0.901 %	3.561 %
RNN	<i>0.066</i> %	0.422 %	1.197 %	1.348 %	3.033 %
LSTM	0.100 %	2.275 %	2.844 %	2.036 %	7.255 %
CNN	0.078 %	0.216 %	0.270 %	0.265 %	0.829 %
RCNN	0.116 %	<i>0.177</i> %	<i>0.227</i> %	0.283 %	0.803 %

Note: Numbers in Bold and Italic fonts represent the lowest error in column; Bold fonts refer to the second lowest error.

However, a few problems in Figure 10 are noteworthy. First, all DL models seem to underestimate the water stages to some extent. Second, the RNN and LSTM models generate consistently bigger spike errors with the increase of prediction length. This problem is not obvious when the prediction length is small (see Figure 10a). However, this problem is less pronounced with MLP and CNN models. Lastly, even though our combined model (RCNN) gives the best performance among all models, its spike errors are not always the lowest.

3.1.2 Comparing performance of models at different locations

In this section, we discuss the prediction results for 24 hours at different locations. Table 5 shows the MAE of the results with the DL models for 24 hours at four locations (S1, S25A, S25B, S26). The MAEs of HEC-RAS simulation results are also provided for comparison. The DL models display smaller MAE values than HEC-RAS for all locations. RCNN model ranked 1st or 2nd for locations (S1, S25A, S25B) while RNN performed best for location S26. Predicting water stage for station S26 had the highest errors.

Table 5. Mean absolute error (MAE) of the predicted results for 24 hours at four different locations for the test set.

	S1	S25A	S25B	S26
MLP	0.160	0.106	0.105	0.259
RNN	0.135	0.139	0.150	0.170
LSTM	0.146	0.136	0.160	0.167
CNN	0.107	0.093	0.090	0.206
RCNN	<i>0.072</i>	<i>0.085</i>	<i>0.082</i>	0.182
HEC-RAS	0.176	0.182	0.198	0.187

Note: Numbers in Bold and Italic fonts represent the lowest error in column; Bold fonts refer to the second lowest error.

Table 6. Percentage of actual prediction errors beyond the range (-0.5, 0.5) feet for 24 hours ahead at four different locations in test set (2019-2020)

	S1	S25A	S25B	S26
MLP	0.208 %	0.229 %	0.322 %	2.847 %
RNN	0.961 %	1.455 %	1.704 %	1.273 %
LSTM	2.364 %	1.320 %	2.883 %	1.579 %
CNN	0.109 %	0.208 %	0.218 %	0.525 %
RCNN	<i>0.094</i> %	0.338 %	0.327 %	0.374 %
HEC-RAS	2.599 %	3.248 %	4.417 %	3.585 %

Note: Numbers in Bold and Italic fonts represent the lowest error in column; Bold fonts refer to the second lowest error.

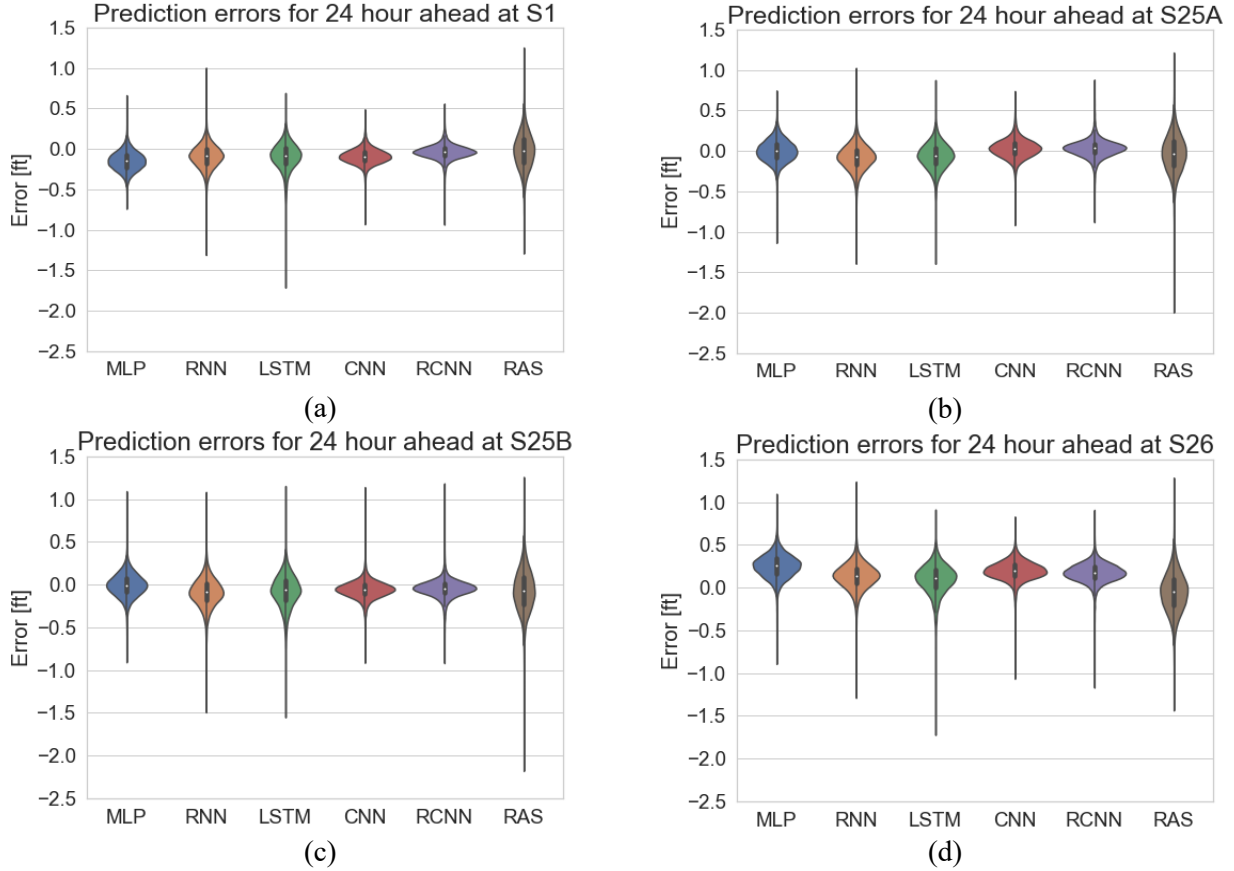


Figure 11. Violin plots of error distributions for 24 hours at each of four locations.

The density distribution of prediction errors for 24 hours is shown in [Figure 11](#). Prediction errors vary with locations, but the common characteristic is the small percentage of spike errors for both DL models and the physics-based HEC-RAS model. DL models MLP, CNN, and RCNN outperform the HEC-RAS model with smaller spike errors at all locations. More importantly, DL models display lower percentage of prediction errors than HEC-RAS. Details of actual predictions errors can be found in [Table 6](#). According to [Figure 11](#) and [Table 6](#), we conclude that all DL models display lower number of prediction errors outside the range $(-0.5, 0.5)$ feet as compared to HEC-RAS. RCNN model displayed the biggest “belly” around the zero position, suggesting that the RCNN model has the most stable and least predictions errors. Note that for the location S25A, RCNN had relatively low errors but was not the best performing model.

3.2 Result visualizations

In this section, we present visualizations of the observed and predicted water stages at each location. We visualize observed and predicted water stages for two short periods, one without a storm event (April 1, 2019) and another with a storm event (August 1-3, 2020).

3.2.1 Normal time period without a storm event

[Figure 12](#) shows the observed water stages, predicted water stages (using the DL models), and the simulated water stages (using HEC-RAS) at four locations on April 1, 2019, which had no storm events. Both DL and HEC-RAS models showed good agreement with the observed data. All models matched well for shorter prediction lengths, but the differences between the models became apparent for longer prediction lengths. DL models performed better than the HEC-RAS model at S1, S25A, and S25B, but not at S26.

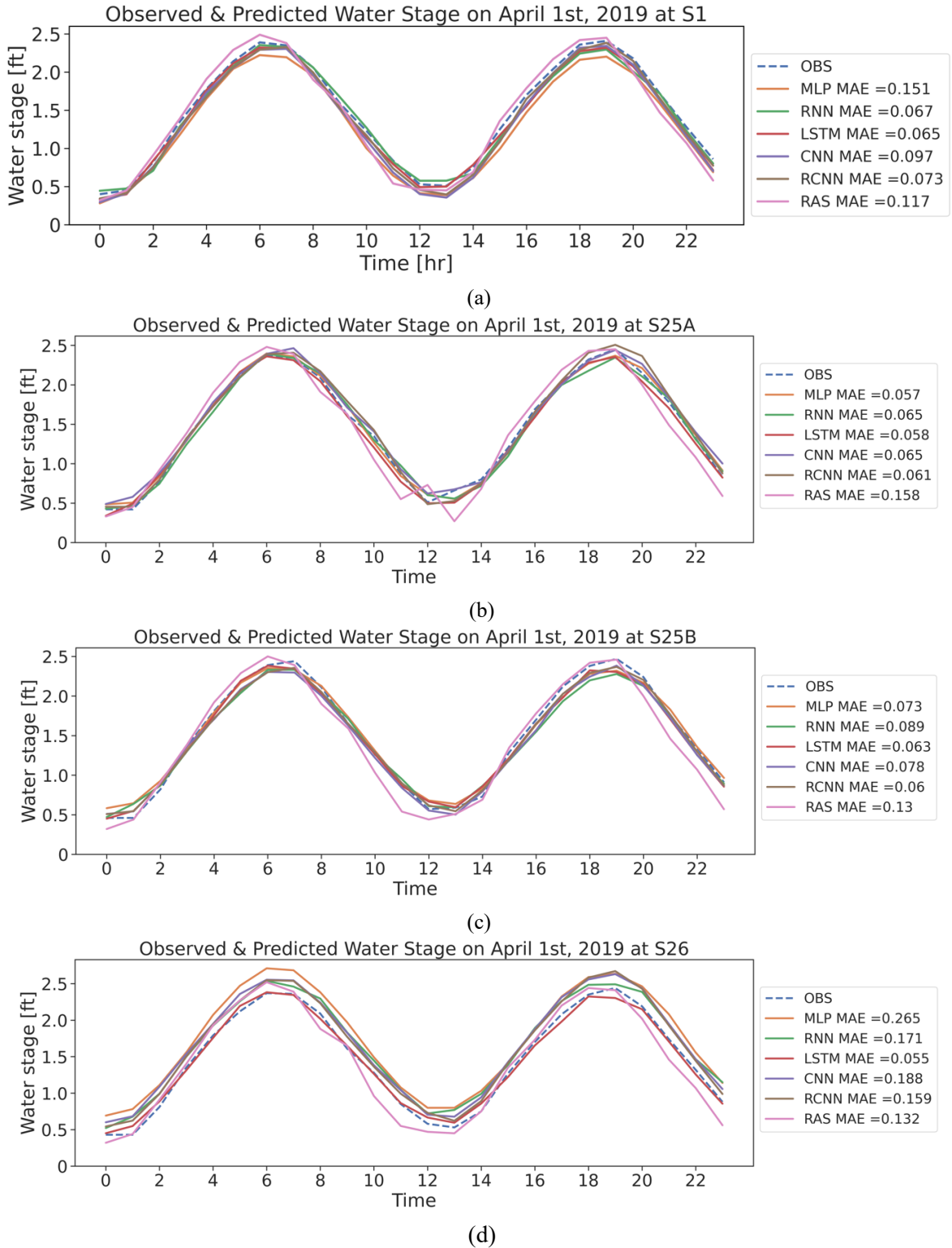
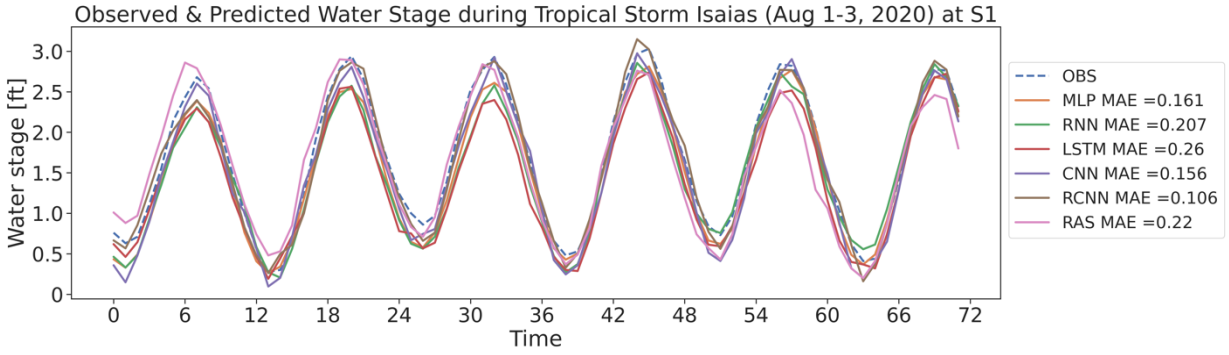
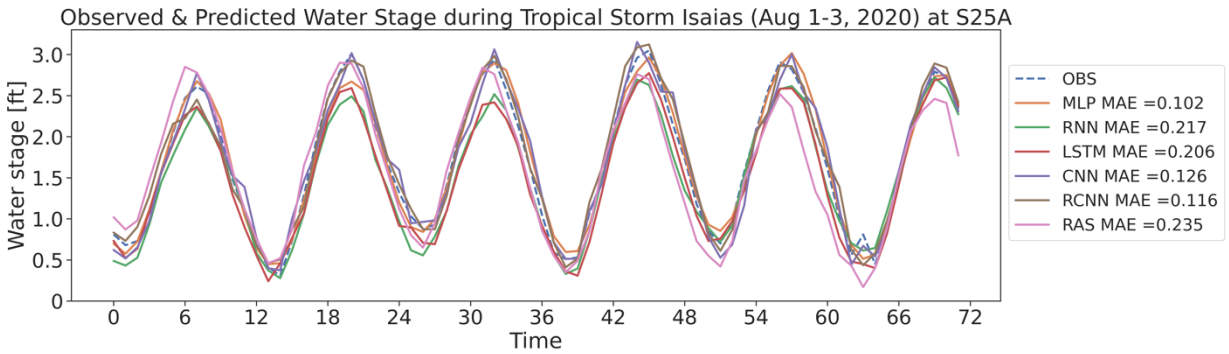


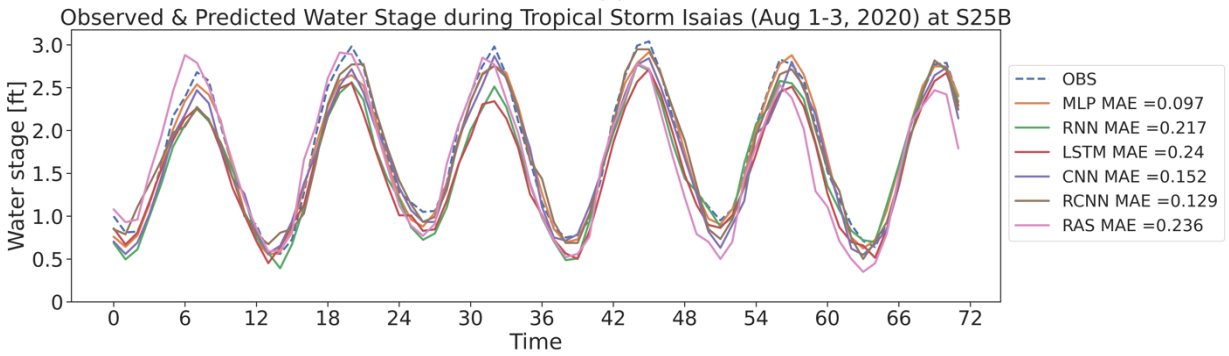
Figure 12. Observed & Predicted Water Stage at 4 locations on April 1, 2019: (a) Water Stage at S1; and Tailwater stages at stations (b) S25A; (c) S25B; and (d) S26.



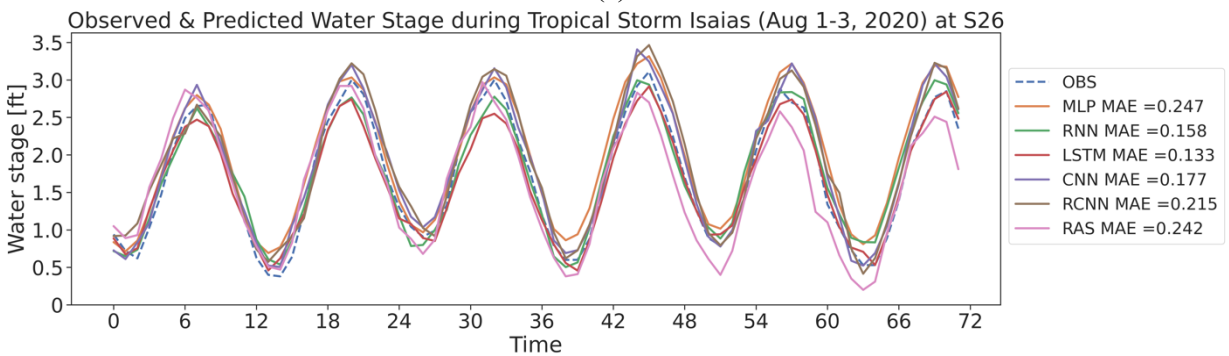
(a)



(b)



(c)



(d)

Figure 13. Observed and Predicted Water Stages for following 24 hours at 4 stations during Tropical Storm Isaias (2020): (a) Water Stage at S1; Tailwater stages at (b) S25A; (c) S25B; and (d) S26.

3.2.2 Period with extreme storm event

The flow rates and water stages in the river rise sharply during a heavy storm event. Accurately predicting the water stages is critical during such periods, ML models that rely only on past information cannot perform well during these periods. During training, our DL models are trained by providing them with covariates from the future – this is fair because these covariates can be reliably predicted even if they were not known. In this work, we used around 9 years of historical data to train the DL models. The training dataset included extreme events like Hurricane Irma (2017), tropical storm Andrea (2013), Hurricane Sandy (2012), and tropical storm Isaac (2012). Tropical storm Isaias (2020) was used to test the accuracy of the models. The tropical storm Isaias reached the greater Miami region on August 1, 2020 and passed about 30-40 miles east of the Palm Beach County coast on August 2, 2020. Thus, we used the period of August 1-3, 2020, to visualize the observed and predicted results.

The predictions for 24 hours into the future at the four locations during tropical storm Isaias are shown in [Figure 13](#). Compared to the normal condition shown in [Figure 12](#), the water stages during tropical storm Isaias are higher. Meanwhile, the MAE values for all models in this set of experiments are slightly higher compared to the experiments in Section 3.2.1. However, all DL models outperformed the HEC-RAS model, with RCNN continuing to rank 1st or 2nd during the storm at locations S1, S25A, and S25B, but not S26.

3.3 Model response to boundary condition changes

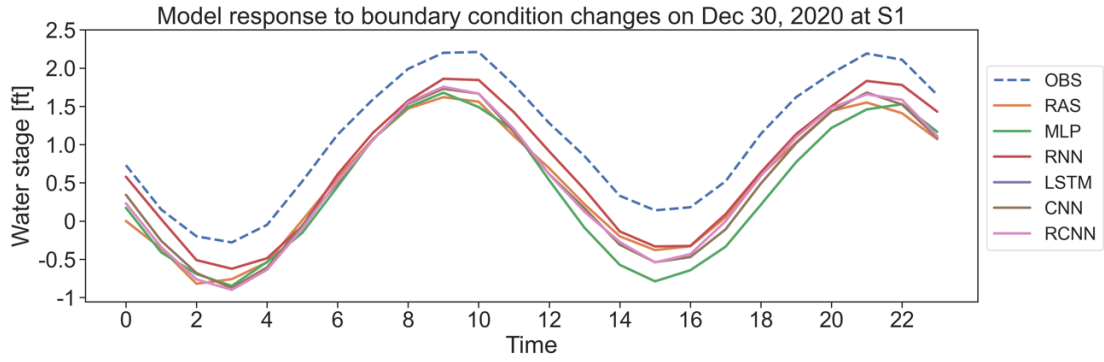
The cross-sectional flow rates and water stages in the river system are completely dependent on the boundary conditions. The correct model response to boundary condition changes is significant for our optimal flood management because we need to frequently change the controllable boundary conditions (gate flow or pump flow) to find the optimal conditions during the optimization stage. Accurately predicting the changes of water stages with the changes in boundary conditions is straightforward for numerical models (e.g., HEC-RAS), but is challenging for conventional DL models that predict the future results based only on the past values and learned trends. To overcome this problem, we incorporated both past information and future covariates (physical boundary conditions) as input so that DL models can utilize this information as well. To test the accuracy of models' responses due to boundary conditions changes, the boundary conditions on December 30, 2020 were manually changed. We reduced spillway gate flows at S26, S25B to 1/10, and set pump flows at S26, S25B to 0. The rainfall intensity, water stage at S4, and spillway gate flow at S25A were kept as in the original historical data. The HEC-RAS simulation was conducted based on the modified boundary conditions as a reference.

3.4 Computation time

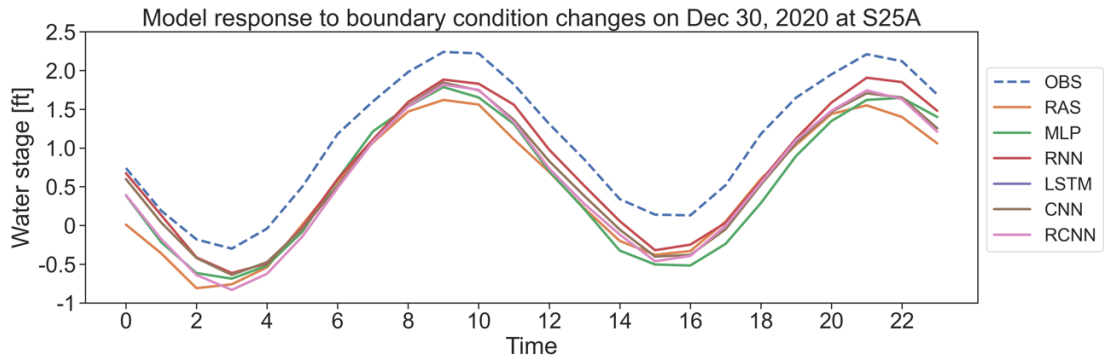
Rapidly predicting water stage is crucial, if these tools are to be used during real-time operations and with different hypothetical boundary conditions (i.e., different gate flow, pump flow, rainfall intensity, tide). [Table 7](#) compares the run times for the DL models in their test phase with HEC-RAS. The training phase is a one-time cost and needs to be included here.

Table 7. Training and test time for all models

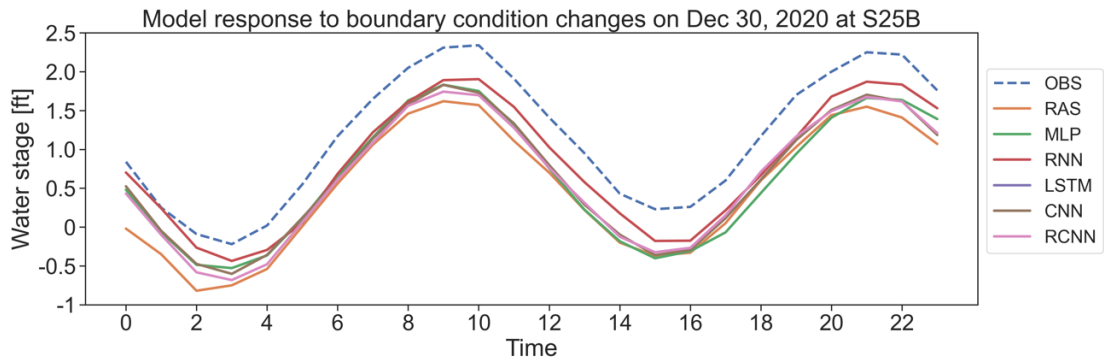
	HEC-RAS	MLP	RNN	LSTM	CNN	RCNN
Training time	-	27 mins	267 mins	1033 mins	167 mins	667 mins
Test time	45 min	0.34 s	1.81 s	4.81 s	0.62 s	2.41 s



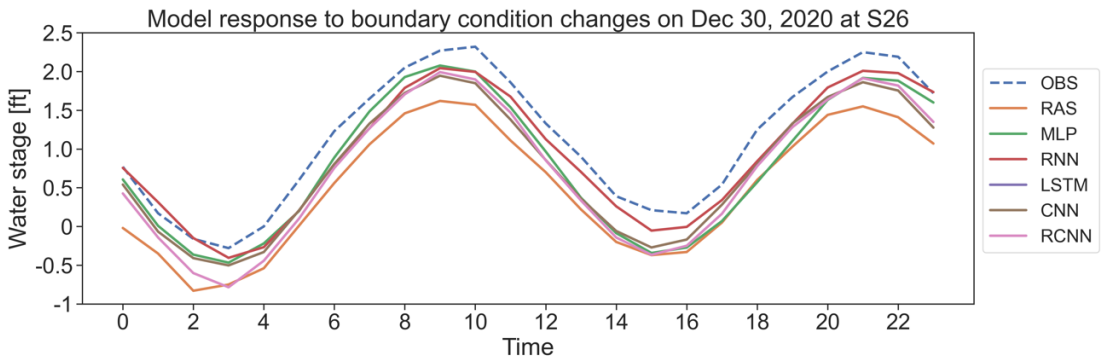
(a)



(b)



(c)



(d)

Figure 14. Predicted water stages changes when the boundary conditions change: (a) Water Stage at S1; Tailwater stages at (b) S25A; (c) S25B; and (d) S26.

All model outputs based on this modified boundary condition are shown in [Figure 14](#). The water stages at all four locations have an obvious decrease because we reduced the upstream flow. The outputs from all DL models were in good agreement with the HEC-RAS reference result and lower than the original observed water stage, thus suggesting that the DL models respond well to changes in the future covariates for their predictions. Note that DL models do not immediately respond to the change (see the first 2-5 timesteps in Figure 14).

4. Discussion and Conclusions

Several DL models were developed and tested to predict water stages at specific locations in the river. Table 7 shows the execution time of the DL models is much lower than the HEC-RAS model, thus bringing us closer to building real-time prediction tools for more complex tasks. Fast response of models generates many implications for the applications in real life. In terms of the model accuracy, all DL models in our paper shows a good agreement with the observed data beside station S26. This may have to do with how precipitation water enters the river system or may be due to variables that are not measured. In addition, all DL models tend to slightly underestimate the water stages much more than they overestimate. This is harmful since it may lead to under preparedness for flood events. This will require explicit corrections in practice. Furthermore, even the maximum or spike errors happen in a couple of time steps, we should pay attention to them since they could be occurring during times of floods and may be the most harmful in practice. In our future work, we aim to deal such a small proportion of spike errors. DL models respond accurately to changes in boundary conditions, but not initially. This delayed response may be improved by using smaller time intervals. This problem is worthy of further investigation in the future.

The key conclusions have been listed as follows. First, compared with HEC-RAS model, the DL models display smaller prediction errors. The RCNN model ranked 1st or 2nd among all models in terms of prediction errors for different prediction lengths and at different locations. Second, DL models such as RNN and LSTM were more sensitive to the prediction length, with higher prediction errors for greater prediction lengths. However, MLP, CNN, RCNN models were relatively insensitive. Thus, most models performed adequately for small prediction lengths, while RCNN model is better for longer prediction lengths. Third, the utilization of future covariates can enhance performance. By combining the past information in a river system and future covariates (boundary condition in HEC-RAS), the DL models predict the water stages during the extreme storm events (e.g., during Tropical storm Isaias in 2020) with only a small increase in error. Fourth, DL models in our paper speed up at least 500x than HEC-RAS.

Data Availability Statement

Some or all data, models, or code generated or used during the study are available in a repository or online in accordance with funder data retention policies. Link: <https://github.com/JimengShi/DL-WaLeF>.

Acknowledgments

This work was partly supported by a grant to GN from the National Science Foundation under the HDR DIRSE program (OAC-2118329), and to AL from the ENG/CBET program (2203292).

References

- Azzi, Z., Matus, M., Elawady, A., Zisis, I., Irwin, P., & Gan Chowdhury, A. (2020). Aeroelastic Testing of Span-Wire Traffic Signal Systems. *Frontiers in Built Environment*, 6, 111.
- Abdalla, E. M. H., Pons, V., Stovin, V., De-Ville, S., Fassman-Beck, E., Alfredsen, K., & Muthanna, T. M. (2021). Evaluating different machine learning methods to simulate runoff from extensive green roofs. *Hydrology and Earth System Sciences Discussions*, 1-24.
- Adnan, R. M., Petroselli, A., Heddam, S., Santos, C. A. G., & Kisi, O. (2021). Short term rainfall-runoff modelling using several machine learning methods and a conceptual event-based model. *Stochastic Environmental Research and Risk Assessment*, 35(3), 597-616.
- Amasyali, K., & El-Gohary, N. (2017). Deep learning for building energy consumption prediction. In 6th CSCE-CRC International Construction Specialty Conference 2017-Held as Part of the Canadian Society for Civil Engineering Annual Conference and General Meeting 2017 (pp. 466-474). Canadian Society for Civil Engineering.
- Alexander, K., Hettiarachchi, S., Ou, Y., & Sharma, A. (2019). Can integrated green spaces and storage facilities absorb the increased risk of flooding due to climate change in developed urban environments?. *Journal of Hydrology*, 579, 124201.
- Borovykh, A., Bohte, S., & Oosterlee, C. W. (2017). Conditional time series forecasting with convolutional neural networks. *arXiv preprint arXiv:1703.04691*.
- Del Campo, F. A., Neri, M. C. G., Villegas, O. O. V., Sánchez, V. G. C., Domínguez, H. D. J. O., & Jiménez, V. G. (2021). Auto-adaptive multilayer perceptron for univariate time series classification. *Expert Systems with Applications*, 181, 115147.
- Goulding, R., Jayasuriya, N., & Horan, E. (2012). A Bayesian network model to assess the public health risk associated with wet weather sewer overflows discharging into waterways. *Water research*, 46(16), 4933-4940.
- Grothmann, T., & Reusswig, F. (2006). People at risk of flooding: Why some residents take precautionary action while others do not. *Natural hazards*, 38(1), 101-120.
- Hirabayashi, Y., & Kanae, S. (2009). First estimate of the future global population at risk of flooding. *Hydrological research letters*, 3, 6-9.
- Hydrologic Engineering Center. (2016). HEC-RAS, River Analysis System, Hydraulic Reference Manual - Version 5.0. <https://www.hec.usace.army.mil/software/hec-ras/documentation/HEC-RAS%205.0%20Reference%20Manual.pdf>
- Huber, W. (1985). Storm Water Management Model (SWMM). Athens, Ga.: Environmental Research Laboratory, Office of Research and Development, U.S. Environmental Protection Agency.
- Keren, G., & Schuller, B. (2016, July). Convolutional RNN: an enhanced model for extracting features from sequential data. In *2016 International Joint Conference on Neural Networks (IJCNN)* (pp. 3412-3419). IEEE.
- Kim, H. I., & Kim, B. H. (2020). Flood Hazard Rating Prediction for Urban Areas Using Random Forest and LSTM. *KSCE Journal of Civil Engineering*, 24(12), 3884-3896.
- Kisi, O., Choubin, B., Deo, R. C., & Yaseen, Z. M. (2019). Incorporating synoptic-scale climate signals for streamflow modelling over the Mediterranean region using machine learning models. *Hydrological Sciences Journal*, 64(10), 1240-1252.
- Kiprijanovska, I., Stankoski, S., Ilievski, I., Jovanovski, S., Gams, M., & Gjoreski, H. (2020). Houseec: Day-ahead household electrical energy consumption forecasting using deep learning. *Energies*, 13(10), 2672.
- Kusler, J. (2004). Multi-objective wetland restoration in watershed contexts. Technical Report.
- Leon, A. S., Tang, Y., Qin, L., & Chen, D. (2020). A MATLAB framework for forecasting optimal flow releases in a multi-storage system for flood control. *Environmental Modelling & Software*, 125, 104618.

- Leon, A. S., Bian, L., & Tang, Y. (2021). Comparison of the genetic algorithm and pattern search methods for forecasting optimal flow releases in a multi-storage system for flood control. *Environmental Modelling & Software*, 145, 105198.
- Mynett, A. E., & Vojinovic, Z. (2009). Hydroinformatics in multi-colours—Part red: Urban flood and disaster management. *Journal of Hydroinformatics*, 11(3-4), 166-180.
- NASA. (2017). Earth observatory: how will global warming change earth? URL: <https://earthobservatory.nasa.gov/Features/GlobalWarming/page6.php>
- Okaka, F. O., & Odhiambo, B. (2018). Relationship between flooding and out break of infectious diseases in Kenya: a review of the literature. *Journal of environmental and public health*, 2018.
- Parhi, P. K. (2018). Flood management in Mahanadi Basin using HEC-RAS and Gumbel's extreme value distribution. *Journal of The Institution of Engineers (India): Series A*, 99(4), 751-755.
- Rivett, M. O., Tremblay-Levesque, L. C., Carter, R., Thetard, R. C., Tengtenga, M., Phoya, A., ... & Kalin, R. M. (2022). Acute health risks to community hand-pumped groundwater supplies following Cyclone Idai flooding. *Science of the Total Environment*, 806, 150598.
- Sadler, J. M., Goodall, J. L., Morsy, M. M., & Spencer, K. (2018). Modeling urban coastal flood severity from crowd-sourced flood reports using Poisson regression and Random Forest. *Journal of hydrology*, 559, 43-55.
- Sajedi-Hosseini, F., Choubin, B., Solaimani, K., Cerdà, A., & Kavian, A. (2018). Spatial prediction of soil erosion susceptibility using a fuzzy analytical network process: Application of the fuzzy decision making trial and evaluation laboratory approach. *Land degradation & development*, 29(9), 3092-3103.
- Shi, J., Jain, M., & Narasimhan, G. (2022). Time Series Forecasting Using Various Deep Learning Models. *International Journal of Computer and Systems Engineering*, 16(6), 224-232.
- Shi, J., Myana, R., Stebliankin, V., Shirali, A., & Narasimhan, G. (2023). Explainable Parallel RCNN with Novel Feature Representation for Time Series Forecasting. arXiv preprint arXiv:2305.04876.
- Tamiru, H., & Dinka, M. O. (2021). Application of ANN and HEC-RAS model for flood inundation mapping in lower Baro Akobo River Basin, Ethiopia. *Journal of Hydrology: Regional Studies*, 36, 100855.
- The Academy by DHI. (2023). MIKE Powered by DHI. <https://www.mikepoweredbydhi.com/>
- Yamak, P. T., Yujian, L., & Gadosey, P. K. (2019, December). A comparison between arima, lstm, and gru for time series forecasting. In *Proceedings of the 2019 2nd International Conference on Algorithms, Computing and Artificial Intelligence* (pp. 49-55).
- Yin, Z., Zahedi, L., Leon, A.S., Amini, M.H. and Bian, L., A Machine Learning Framework for Overflow Prediction in Combined Sewer Systems. In *World Environmental and Water Resources Congress 2022* (pp. 194-205).
- Zhang, R., Zen, R., Xing, J., Arsa, D. M. S., Saha, A., & Bressan, S. (2020). Hydrological Process Surrogate Modelling and Simulation with Neural Networks. *Advances in Knowledge Discovery and Data Mining*, 12085, 449.
- Zhao, G., Pang, B., Xu, Z., Peng, D., & Xu, L. (2019). Assessment of urban flood susceptibility using semi-supervised machine learning model. *Science of the Total Environment*, 659, 940-949.